PHYSICAL REVIEW C VOLUME 40, NUMBER 3 SEPTEMBER 1989

Optical potentials for alpha particles on Ca isotopes at 1.37 GeV

M. Nakano, H. Matsuura, and T. Maki
University of Occupational and Environmental Health, Japan, Kitakyushu 807, Japan

M. Matoba and H. Ohgaki
Graduate School of Engineering Sciences, Kyushu University, Kasuga 816, Japan
(Received 13 October 1988; revised manuscript received 31 May 1989)

A phenomenological optical-model analysis is performed for the elastic scattering of alpha particles on ^{40,42,44,48}Ca at 1.37 GeV. Two geometries are considered for optical potentials, i.e., the traditional Woods-Saxon form and the double-Woods-Saxon form which can represent a change of the potential shape from the Woods-Saxon one. Among them, the best-fit potential has a "Mexican-hat" shape which is characterized by a long-ranged and weak attractive part in the surface region and a repulsion in the central region. From discussions on shape dependence of chi-square values, reaction cross sections, volume integrals, notch tests, and global potentials, a reasonable shape of the real part of the optical potential is suggested to be the "Mexican-hat" shape at this energy.

I. INTRODUCTION

The optical model has played a remarkable role in describing nuclear scattering phenomena. For proton-nucleus scattering, it has been shown that the potential shape apparently changes from a Woods-Saxon (WS) shape at low energies (<80 MeV/nucleon) to a wine-bottle-bottom (WBB) shape at intermediate energies (~ 200 MeV/ nucleon).[1-3]

Also, it has recently been demonstrated, albeit phenomenologically; that the real central potential shape changes in deuteron scattering on ^{16}O at 700 MeV (350 MeV/nucleon).[4] It is of interest to investigate how this "shape change" persists in the scattering of various composite particles. However, optical-model analyses of high-energy heavy-ion scattering data are still few.

For alpha particles, Bonin *et al.* measured the elastic scattering on ^{58}Ni, ^{116}Sn, and ^{208}Pb at 288, 340, 480, and 699 MeV, and searched optical potentials with conventional WS shapes.[5] Maki *et al.* analyzed the same data without this restriction and showed that the shape of optical potentials is likely to change from a WS shape to a WBB shape as the incident energy increases.[6]

Thus, it is interesting to study the optical potentials for alpha-particle scattering at higher energies and to examine whether this shape change persists or not. In 1977, Alkhazov *et al.* measured the elastic scattering cross sections of alpha particles on Ca isotopes at 1.37 GeV using the Saturne synchrotron at Saclay.[7] They analyzed the data using the Glauber model.[7,8] Although this model reproduced the experimental data very well, the shape of the optical potential could not be determined. It is noteworthy that this energy (343 MeV/nucleon) coincides with that around which the $p+$Ca potential changes shape, and also with the energy of the $d+^{16}$O experiment in Ref. 4.

These data are suitable for optical potential analysis because the angular distributions were measured in small angular steps (0.25°) with a relatively small error (10%). The analysis of these data leads us to examine whether the optical model is meaningful for the interpretation of the experiments at this higher energy, and if so what types of potentials are suggested from the experimental side as reasonable for the scattering of alpha particles at the intermediate energy (343 MeV/nucleon). This work is aimed at examining these two questions. As a result, a clear preference for a particular shape of the real part of the optical potential is demonstrated.

In Sec. II, two geometries of the optical potentials employed in our search of best-fit potentials are described. It is emphasized that special care is necessary to ensure the accuracy of calculations. In Sec. III, we examine the sensitivity of the data set to the shape of the potential. The crucial evidence is presented by a study of the shape dependence of the chi-square values. This is demonstrated with a plot of the best attainable chi squares as a function of the shape of the real part of the potential. Global potential sets are determined on the assumption of smooth isotope dependence of the potential parameters. A notch perturbation test is carried out to examine the sensitivity of the real potential in relation to the distance from the nuclear interior. The role of the imaginary potential, which renders the fits insensitive to the interior real well depth, is discussed. A comparison of the deduced potential sets is made with respect to the reaction cross sections and the volume integrals of the potentials. In Sec. IV, the obtained potential sets are also compared with the potential predicted on the basis of Brueckner theory, and conclusions are given.

II. OPTICAL POTENTIAL SEARCH UNDER TWO GEOMETRIES

A. Reconstruction of the data and the accuracy of the numerical calculation

The measured angular distributions are diffractive in the narrow angular range, and it is quite difficult to measure the data at deep minima. Thus it is necessary to make some corrections to the raw data obtained by the

spectrometer with position and cutting-angle-sensitive detectors. The details of the angular distribution reconstruction procedure are described in Ref. 9.

The numerical calculations require special attention. We need angular distributions calculated to an accuracy of at least 10^{-7} because the absolute cross sections fall off rapidly in the narrow range of the angles. At first, we should determine the maximum value of angular momentum (l_m) in this analysis. This is important because angular momenta of partial waves used in the high-energy heavy-ion scattering are considered to be large. It depends on the incident energy and the range of the interaction. This value must be determined to render the S matrix reasonably convergent. We carefully checked the change in the S matrices and angular distributions by increasing l_m in steps of 10 units. The distribution patterns calculated for $l_m = 100$, 150, 200, and 250, along with the experimental data are shown in Fig. 1. As can be seen in Fig. 1(a), smaller l_m (<200) fails to reproduce the distribution at higher angles. It was concluded that $l_m = 250$ is more than adequate for our purposes, as it exhibits a regular diffraction pattern for $\theta \lesssim 20°$ and reproduces all observed maxima and minima. Other important parameters are the matching radius (R_m) and the mesh size (dR) for integration. From Fig. 1(b), it becomes clear that $R_m = 15$ fm and $dR = 0.015$ fm is sufficient for our data

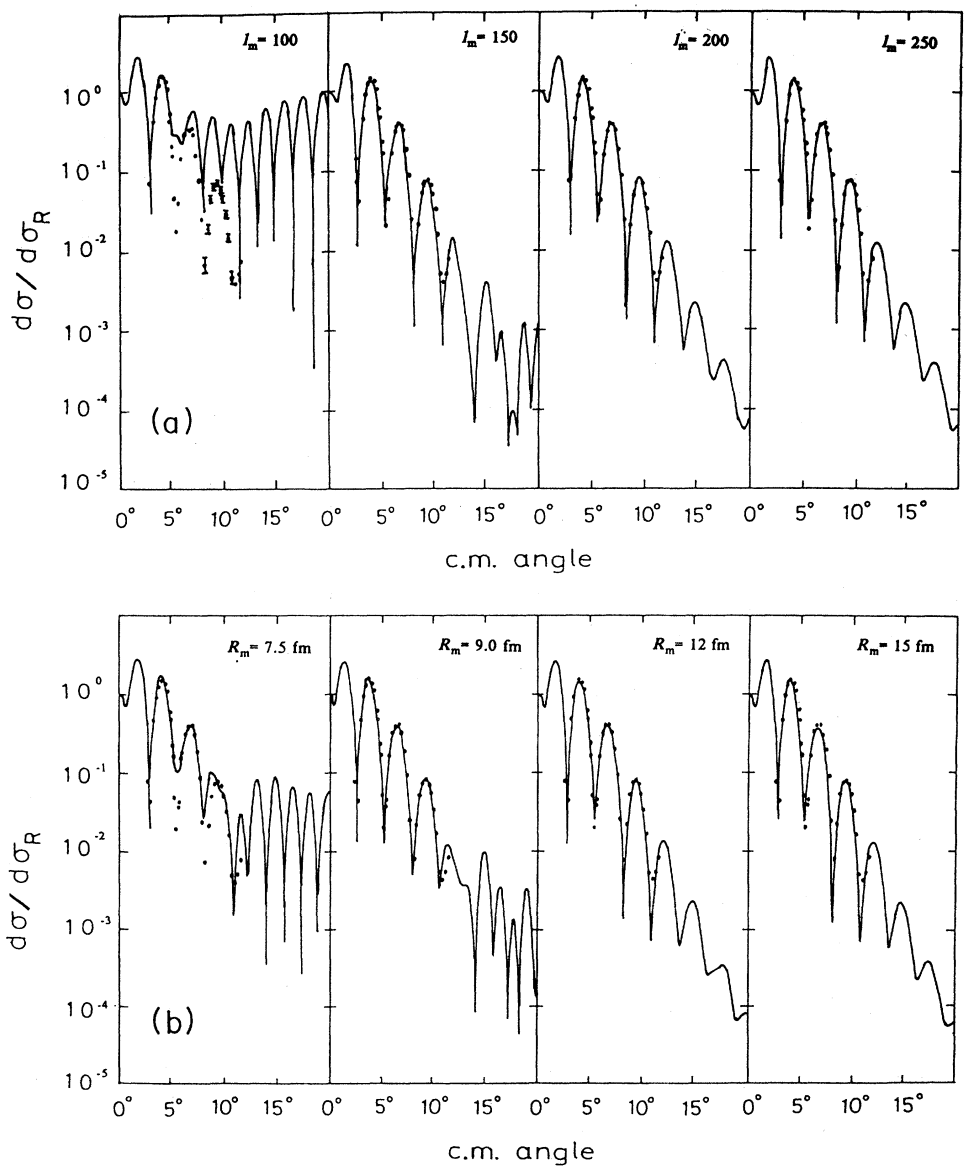

FIG. 1. Convergence in angular distributions for the various maximum clauses of angular momentum (l_m) and matching radius (R_m). The upper panels show four cases of $l_m = 100$, 150, 200, and 250, and the lower panels show four cases of $R_m = 7.5$, 9, 12, and 15 fm from the left-hand side. The angular distributions are presented by the ratios of the elastic cross sections to the Rutherford cross sections and plotted as a function of the center-of-mass angle. As an example, this calculation is made for the $\alpha + {}^{40}$Ca system using the global potential parameters of the Mexican-hat shape in Table IV.

set. Thus the following analyses employ the same set of parameters.

B. Standard Woods-Saxon form

The potential search is made with two geometries for the shape of the real part of the optical potential. One is the traditional Woods-Saxon (WS) form and the other is the Woods-Saxon plus squared Woods-Saxon one which is, hereafter, cited as the "double-Woods-Saxon" (DWS) form. This DWS form has six parameters for the real part, and it can represent various shapes including the simple Woods-Saxon shape, the wine-bottle-bottom shape, and others which are classified in Fig. 2. Although the DWS form includes a WS shape, the search in the WS form was made independently.

The Woods-Saxon potential is written as follows:

$$U^{\mathrm{WS}}(r)=Vf(r_R,a_R;r) +iWf(r_I,a_I;r)+V^{\mathrm{Coul}}(r_C;r)\ , \quad (1)$$
$$f(r_0,a_0;r)=1/\{1+\exp[(r-R)/a_0]\},\quad R=r_0A_T^{1/3},$$

with the Coulomb radius parameter $r_c=1.3$ fm and A_T the mass number of the target nucleus.

Only a volume type is adopted for imaginary potentials, since the effects of the surface type are expected to be very small at this energy.[10,11] Thus the WS potential used has six free parameters.

The best-fit results are shown in Fig. 3. The calculated angular distributions are in good agreement with the experimental data. It is worthwhile to mention that the

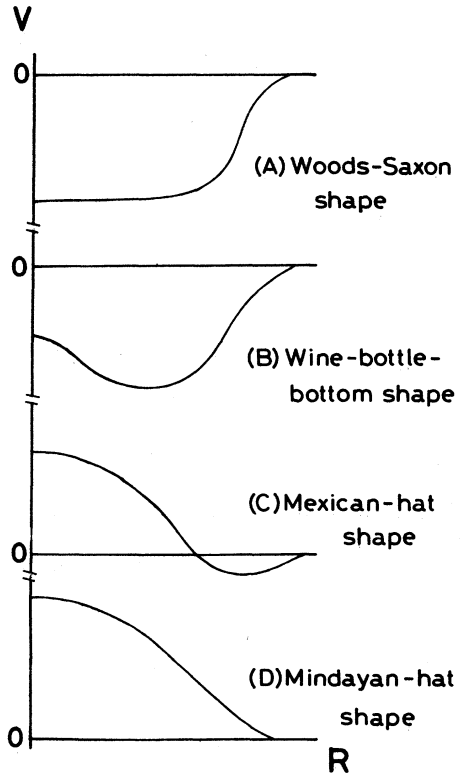

FIG. 2. Gross classification of potential shapes represented by the double Woods-Saxon shape where (*A*), (*B*), (*C*), and (*D*) represent a Woods-Saxon shape, a wine-bottle-bottom shape, a Mexican-hat shape, and a Mindayan-hat shape, respectively. The scales of the axes are arbitrary.

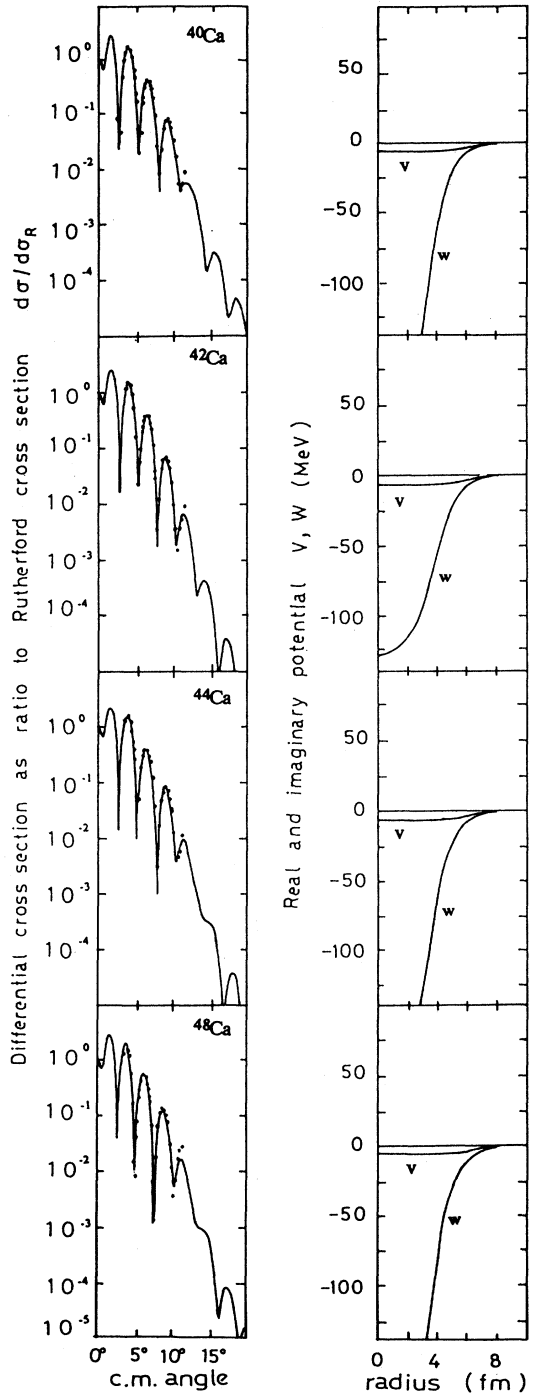

FIG. 3. Best-fit WS potentials with six free parameters and their angular distributions, together with the experimental data of ^{40,42,44,48}Ca from the top. The solid line is the optical-model fit to the data with the searched values given in Table I. As for the error bars of the experimental data, see Fig. 1(a).

TABLE I. Best-fit potential parameters of the Woods-Saxon shape with six free parameters and related quantities such as volume integrals of the real and imaginary parts of the potential, J_R, J_I and reaction cross sections σ_R,

	V (MeV)	r_R (fm)	a_R (fm)	W (MeV)	r_I (fm)	a_I (fm)	χ^2/N	J_R	J_I	σ_R (mb)
^{40}Ca	−6.890	1.841	0.646	−332.7	0.790	0.880	1.42	−49.7	−353.4	1159
^{42}Ca	−7.095	1.828	0.741	−129.8	1.072	0.811	0.69	−51.5	−245.9	1126
^{44}Ca	−6.530	1.783	0.612	−236.3	0.894	0.877	1.26	−42.3	−312.0	1211
^{48}Ca	−5.604	1.750	0.586	−405.9	0.760	0.890	3.68	−34.1	−379.2	1277
							Average = 1.76			

agreement between the data and optical-model fits validates the angular distribution reconstruction from raw data, and also confirms that the optical model is useful at the intermediate energies. The best-fit optical potential parameters are listed in Table I. The range parameters of the imaginary potentials r_I are much smaller than those of the real potentials. This short ranged and deep imaginary potentials have a relation with the ambiguity of the potential. This point is important and will be discussed again in the following sections.

All the best-fit WS potentials have very shallow real parts and deep imaginary parts. This shallow real part results in deeper dips in angular distributions. As is shown in Fig. 4, the dips become more shallow as the real potentials become less attractive. This means that the measurement of the deep minima is also important for fixing the real part of the potential.

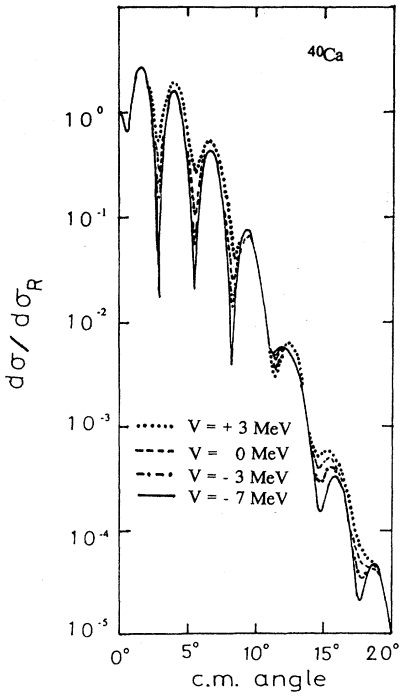

FIG. 4. The role of the real part of the WS potential. Angular distributions are calculated for various depth V, while the other five parameters are kept to the best-fit WS values. The solid line shows the best-fit angular distribution with $V=-6.89$, and the dashed-dotted, dashed, and dotted lines show the angular distributions with $V=-3$, 0, and +3 MeV, respectively.

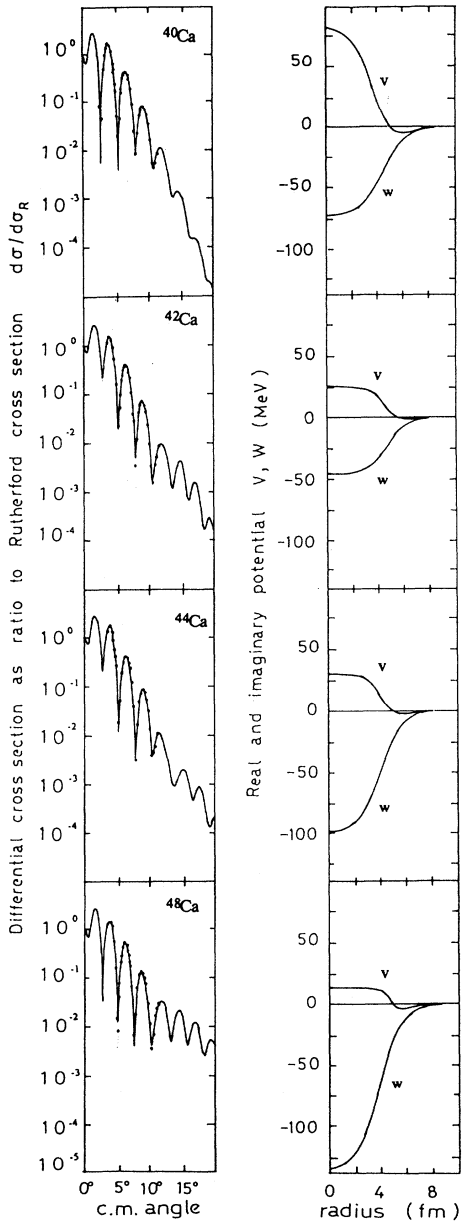

FIG. 5. Best-fit Mexican-hat (MH) potentials with nine free parameters and their angular distributions together with the experimental data. The solid line is the optical-model fit with the searched values given in Tables II.

TABLE II. Best-fit potential parameters of the Mexican-hat (MH) shape with nine free parameters and related quantities such as volume integrals of the real and imaginary parts of the potential, J_R, J_I and reaction cross sections σ_R.

	V (MeV)	r_R (fm)	a_R (fm)	V_2 (MeV)	r_2 (fm)	a_2 (fm)	W (MeV)	r_I (fm)	a_I (fm)	χ^2/N	J_R	J_I	σ_R (mb)
^{40}Ca	−10.701	1.787	1.002	93.86	1.237	0.834	−72.08	1.274	0.864	0.59	53.4	−215.8	1224
^{42}Ca	−0.928	2.025	0.351	26.85	1.384	0.565	−46.97	1.355	0.730	0.29	48.9	−151.3	1054
^{44}Ca	−1.911	1.878	0.412	32.18	1.281	0.586	−100.02	1.141	0.837	1.15	39.7	−222.0	1184
^{48}Ca	−4.405	1.904	0.575	17.13	1.344	0.320	−136.42	1.053	0.879	0.73	2.3	−255.1	1283
										Average=0.69			

C. Double Woods-Saxon form

The double Woods-Saxon form is represented as

$$U^{\mathrm{DWS}}(r)=U^{\mathrm{WS}}(r)+V_2 f^2(r_2,a_2;r)\ , \tag{2}$$

where f^2 is a squared form of the Woods-Saxon shape and V_2 is real and usually positive, i.e., a repulsive force. The imaginary part is kept as a WS shape. Thus the DWS form has nine free parameters.

The best-fit potentials are shown in Fig. 5, and their parameters are listed in Table II; these potentials also reproduce the experimental data well. The shape of the real potential evidently changes from the standard Woods-Saxon shape to the shape which is classified as a "Mexican-hat" shape in Fig. 2. The Mexican-hat (MH) shape is characterized by a long-ranged attraction at the surface and a repulsion in the central region. In contrast to the best-fit WS potential, the imaginary part is not so deep. The range of the imaginary potential of MH shape is smaller than that of the real potential, as well as that of the WS potentials. Both potentials have the "surface transparent" nature which was apparent in the scattering of alpha particles at lower energies.[5] This surface transparent nature makes the nucleus translucent. As shown in Fig. 6, the peaks shift to the forward angles and the angular distributions become more diffractive as the range r_I becomes larger than that of the best fit. The limit of sufficiently deep imaginary potential corresponds to a shadow scattering by a black disk.

The comparison between Fig. 3 and Fig. 5 provides the most notable difference between the two shapes. Even in the region larger than 4 fm, the shapes of the real part are quite different from each other, although the imaginary part is very similar in the outer region. This difference can be seen in angular distributions, as will be shown by the notch test. Actually, it is seen that the WS shape gives a difference at larger angles. Particularly, the heights of the fifth and sixth peaks are lower than those of MH shape in all isotopes. This difference is an important point in the selection of the preferable shape of the real part, as will be shown in the following sections.

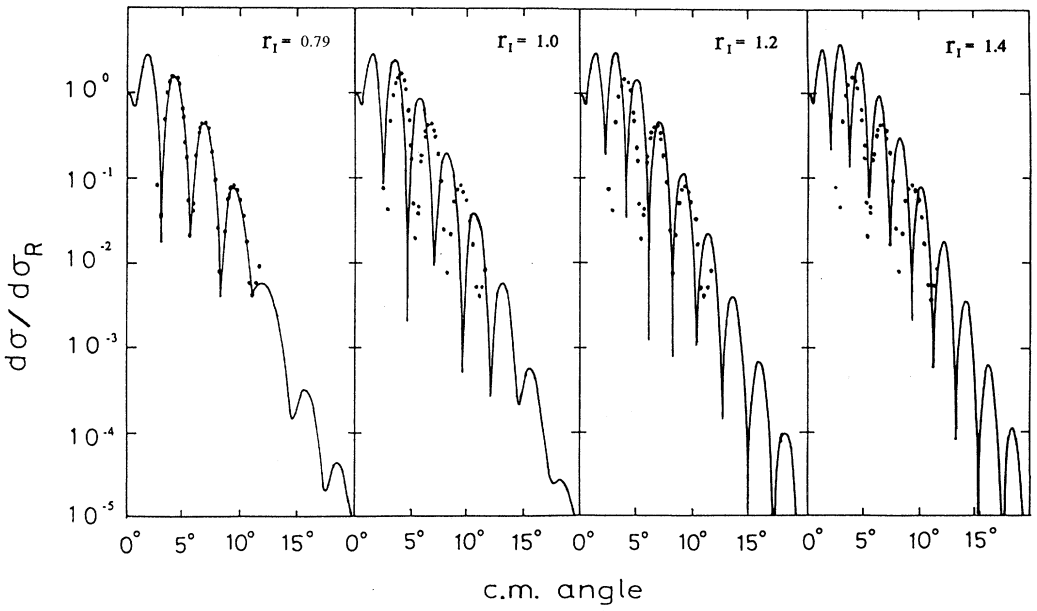

FIG. 6. The change in the angular distributions calculated for increasing the range parameter of the imaginary potential. Four cases of $r_I=0.79$ (best fit), 1.0, 1.2, and 1.4 are shown from the left-hand side. The other five parameters are kept to the best-fit WS values.

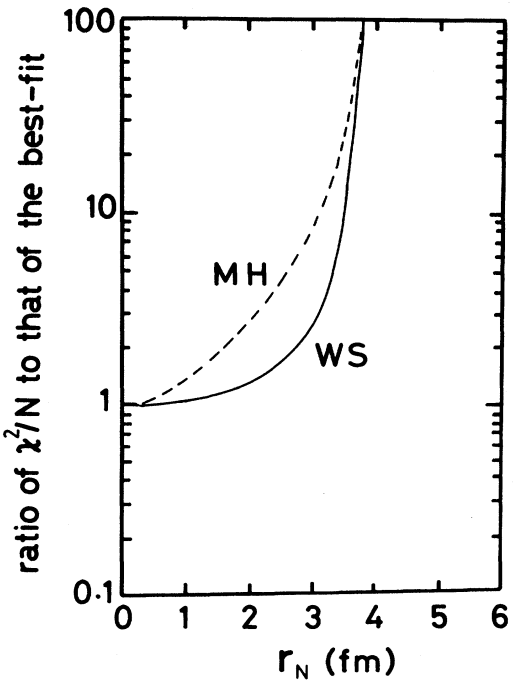

FIG. 7. Ratios of χ^2/N values to the best-fit χ^2/N values in a "notch test" where a small perturbative potential is added whose center is r_N, the depth is 10 MeV, and the diffuseness parameter is 0.2 fm. In our case, the depth is kept constant, in contrast to the usual notch test. The solid and dashed lines show the χ^2/N for the Woods-Saxon and the Mexican-hat potentials, respectively. As an example, this calculation is made for the $\alpha+^{40}$Ca system.

III. DISCUSSION

A. Ambiguity of the searched potentials and notch test

In the preceding section, we obtained two shapes WS and MH which can reproduce the experimental data well. The potential obtained are further scrutinized to see if we can single out a potential shape as the preferred one. We shall discuss the ambiguity of the searched potentials from the following two points; one is a so-called notch test and the other is the shape dependence of the chi square per data point (χ^2/N).

In the notch test, we perturb the searched potential by adding a narrow radial potential which has the variable center r_N, of width 0.2 fm and of constant depth of 10 MeV. The relative ratio of the χ^2/N to that of the best fits are plotted versus the variable center r_N in Fig. 7. The chi square in the case of WS potential does not change substantially even if the small perturbation is added in the inner region less than 3 fm. This indicates that the angular distributions are not sensitive to the shape of the WS potential for $r<3$ fm. The deep and short-ranged imaginary potential of WS, as shown in Fig. 3, is the main contributing factor. On the contrary, the chi square in the case of the MH shape changes gradually even in the inside region. This indicates that the MH shape is determined with a relatively small ambiguity up to the deep interior of the nucleus.

A small perturbation in the outer region ($r>4$ fm) influences chi-square values for both the MH and WS shapes, which proves that the outside region of the potentials is determined with little ambiguity. This is indicated also in Fig. 8, which shows the angular distributions cal-

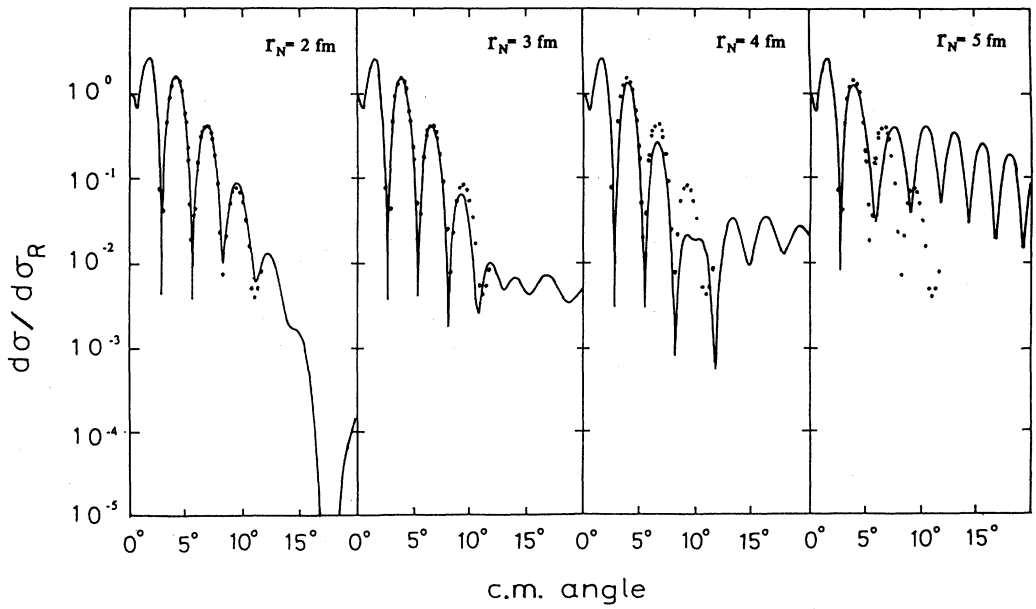

FIG. 8. Angular distributions calculated with various r_N at the notch test. The potential in this calculation is the best-fit MH potential plus the small perturbative potential whose center is r_N. Four cases of $r_N=2$, 3, 4, and 5 fm are shown for the $\alpha+^{40}$Ca system.

culated with the perturbed potentials. The figure shows that the deviation in angular distributions appears at larger angles when we vary the center of the narrow radial potential from outside to inside. The agreement between calculations and the present data set, extending up to 11°, is not influenced by potential variation for $r_N < 3$ fm. Beyond this radius, the experimental data are quite sensitive to the real potential, and we conclude that this analysis with the available data set fixes the shape of the potential from the nuclear surface to about 3 fm.

B. Shape dependence of χ^2/N

As a further test of the above-mentioned results we have examined the shape dependence of χ^2/N in the following way. Fixing the r_2 and a_2 to the best-fit values listed in Table II, a free parameter search was conducted for V, r_R, a_R, W, r_I, and a_I for different values of V_2. The trial with $V_2=0$ is, of course, the traditional WS search. The best attainable χ^2/N, as a function of the depth V_2, is shown in Fig. 9 for all isotopes, together with the potentials obtained. The V_2 for the best χ^2 are quite isotope dependent. It can be seen that the MH shape is favored clearly for ^{48}Ca, and roughly for ^{42}Ca and ^{40}Ca. The valley in the ^{44}Ca case is too broad to identify the shape. This may, at least partly, be due to the limited experimental data. The data of ^{48}Ca have more data points than ^{44}Ca, especially in the fifth peak around 11°, which is very important for the identification of the shape, as discussed in Sec. II. The high peak value

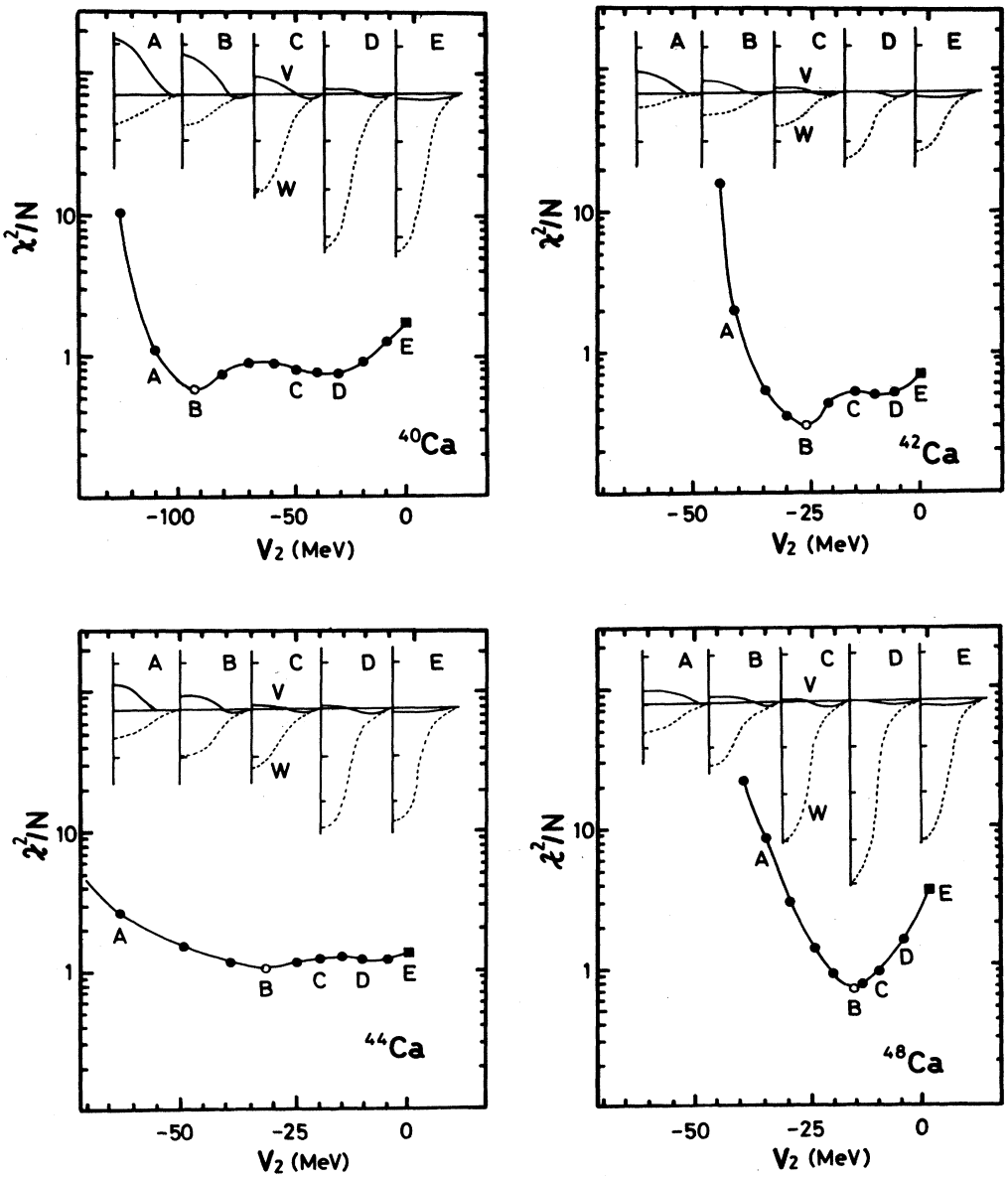

FIG. 9. Best attainable χ^2/N values within the six-parameter search for various V_2, while r_2 and a_2 are kept constant. The dotted points in the figure show the searched values and the solid lines are only to guide the eye. Some of the searched potentials are depicted for the points (A)–(E), where point (B) is the best-fit MH potential and point (E) is the best-fit WS potential.

TABLE III. Global potential parameters for the WS shape and related quantities. The four parameters are fixed to $r_R=1.80$ fm, $a_R=0.65$ fm, $r_I=0.89$ fm, and $a_I=0.86$ fm, and the depth parameters V and W are given by the formula in the text.

	V (MeV)	W (MeV)	χ^2/N	J_R	J_I	σ_R (mb)
^{40}Ca	−7.021	−244.2	5.10	−47.6	−306.1	1150
^{42}Ca	−6.525	−249.0	21.1	−44.1	−307.4	1177
^{44}Ca	−6.028	−254.7	8.88	−40.6	−310.1	1204
^{48}Ca	−5.035	−263.3	36.9	−33.7	−312.5	1254
			Average=18.0			

of ^{48}Ca in the angular distribution can be reproduced only by MH potentials. The reason ^{44}Ca has the broad valley in the χ^2/N is that ^{44}Ca has a few data points in the important fifth peak in the angular distribution, and the height of the peak is not definite.

C. Role of the imaginary potential

Another interesting point in Fig. 9 is the change in the depth of imaginary potentials. The imaginary potential becomes deeper as the real part changes from MH shape to WS shape.

This implies that the imaginary potential masks the effect from the inside region of the WS potential, which is attractive and opposite to the MH potential. As explained in subsection A, the deep imaginary potential renders the fits insensitive to the magnitude and shape of real potential for $r<4$ fm.

D. Global optical potentials

The main criterion for the best-fit potentials is to obtain a minimum χ^2/N without regard to the errors of the experimental data points. As a result, the best-fit potentials do not necessarily exhibit a smooth isotope dependence. However, we can construct global potentials by expecting the smooth isotope dependence of the potential parameters. The global potentials have no free parameters. We determined the parameters as follows. First, we searched the depth parameters V, W (and V_2 for the MH shape), fixing the other parameters r_R, a_R, r_I, a_I (and r_2,a_2 for the MH shape) around their averages of the best-fit parameters. After that, we determined the best-fit linear function of the neutron number N for the depth parameters searched. The formula obtained for the depth parameters is as follows:

(i) For WS shape,

$$V=-7.02+0.25(N-Z),\quad r_R=1.80,\quad a_R=0.65\ ,$$

$$W=-244.0-2.38(N-Z),\quad r_I=0.89,\quad a_I=0.86\ .$$

(ii) For MH shape,

$$V=-9.59+0.41(N-Z),\quad r_R=1.75,\quad a_R=0.85\ ,$$

$$V_2=+41.7+0.04(N-Z),\quad r_2=1.30,\quad a_2=0.66\ ,$$

$$W=-92.0+0.36(N-Z),\quad r_I=1.19,\quad a_I=0.83\ .$$

The χ^2/N and the related quantities are listed in Tables III and IV, and the angular distributions are shown in Figs. 10 and 11 together with the potentials. As shown in the figures, the isotope dependence of the angular distribution and the potentials are very smooth for both shapes. It is clearly seen that the large difference between the WS and MH shapes comes from the fifth peak in the angular distributions. The WS global potentials cannot reproduce the high peak value, while it is reproduced by the MH global potentials. Hence, the average χ^2/N value of the MH global potentials is much smaller than that of WS global potentials. Thus global potentials offer another reason to prefer the MH shape over the WS shape.

One might consider that the global potential for the MH shape differs largely from the best fit MH potential, especially in ^{40}Ca, because the heights of the "hat" are different from each other. However, we should consider the surface region, which greatly influences the angular distributions. The two potentials have little difference in the region $r>4$ fm, although the heights are quite

TABLE IV. Global potential parameters for the MH shape and related quantities. The six parameters are fixed to $r_R=1.75$ fm, $a_R=0.85$ fm, $r_2=1.30$ fm, $a_2=0.66$ fm, $r_I=1.19$ fm, and $a_I=0.83$ fm, and the depth parameters V, V_2, and W are given by the formula in the text.

	V (MeV)	V_2 (MeV)	W (MeV)	χ^2/N	J_R	J_I	σ_R (mb)
^{40}Ca	−9.591	41.68	−92.00	3.68	6.85	−228.2	1091
^{42}Ca	−8.780	41.76	−91.28	5.10	12.9	−224.3	1187
^{44}Ca	−7.968	41.83	−90.56	2.21	18.7	−220.6	1210
^{48}Ca	−6.345	41.98	−89.12	2.60	30.5	−213.7	1255
				Average=3.40			

different in the central region. The difference cannot be noticed if one does not measure more backward angles, for example, the sixth peak. It should be worthwhile to note that the peaks in the angular distribution by the global potential for the MH shape falls off naturally at larger angles beyond 11°, although the χ^2/N values are slightly larger than those of the best fits.

E. Reaction cross sections and volume integrals

In this subsection, we compare other physical quantities such as reaction cross sections or volume integrals of the potentials. There are no experimental data of reaction cross sections of the alpha particles on Ca isotopes in this energy region. However, we can estimate these

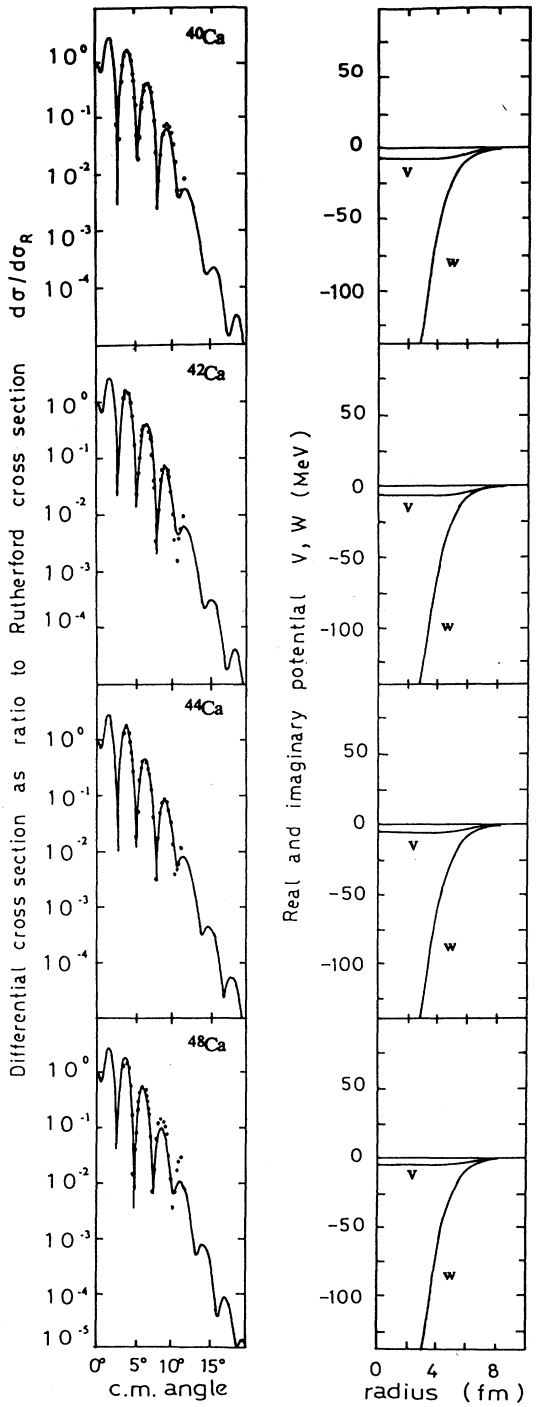

FIG. 10. Global potentials for the WS shape and their angular distributions of ^{40}Ca, ^{42}Ca, ^{44}Ca, and ^{48}Ca from the top.

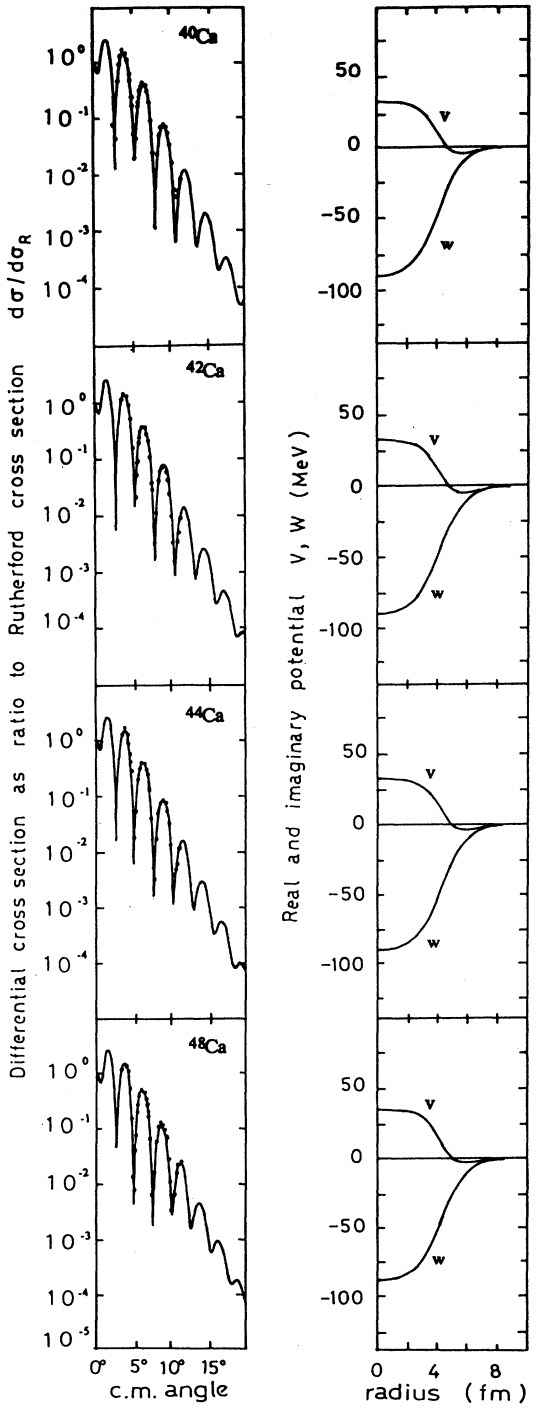

FIG. 11. Global potentials for the MH shape and their angular distributions of ^{40}Ca, ^{42}Ca, ^{44}Ca, and ^{48}Ca from the top.

values from other data. According to Peng *et al.*,[12] the reaction cross section of the alpha particles on ^{12}C is about 550 mb at this energy. Considering the reaction cross sections to be simply due to surface interaction, one can write

$$\sigma_R(A_1)=(A_1/A_2)^{2/3}\sigma_R(A_2) .$$

Thus for Ca isotopes we obtain $\sigma_R=1200$ mb from this estimate. As listed in Tables I and II, all the best-fit potentials give reasonable reaction cross sections close to this value.

The systematics of the volume integrals of the obtained real and imaginary potentials are shown in Fig. 12 together with the systematics for the potentials of composite particles at low energies.[13,14] From the Arnold's line,[15] which is estimated for proton scattering in the intermediate energy region, the volume integral of the real part of the potential should be about 10 MeV fm^3 and the volume integral of the imaginary part is about 210 MeV fm^3 at 343 MeV/nucleon. In the case of the WS shape, the calculated values of the volume integrals of real parts are slightly large (34–52 MeV fm^3), and those of the imaginary part are much larger (245–379 MeV fm^3). In the case of the MH shape, the potentials obtained give slightly small volume integrals for the real potential because of the repulsion in the central region, while the volume integrals of the imaginary potential range over 151–255 MeV fm^3 around the Arnold's line. The situation seems to be better in the MH shape than in the WS shape. Furthermore, the volume integrals of the global MH potentials come very close to the Arnold's line, while the global WS potentials are not compatible.

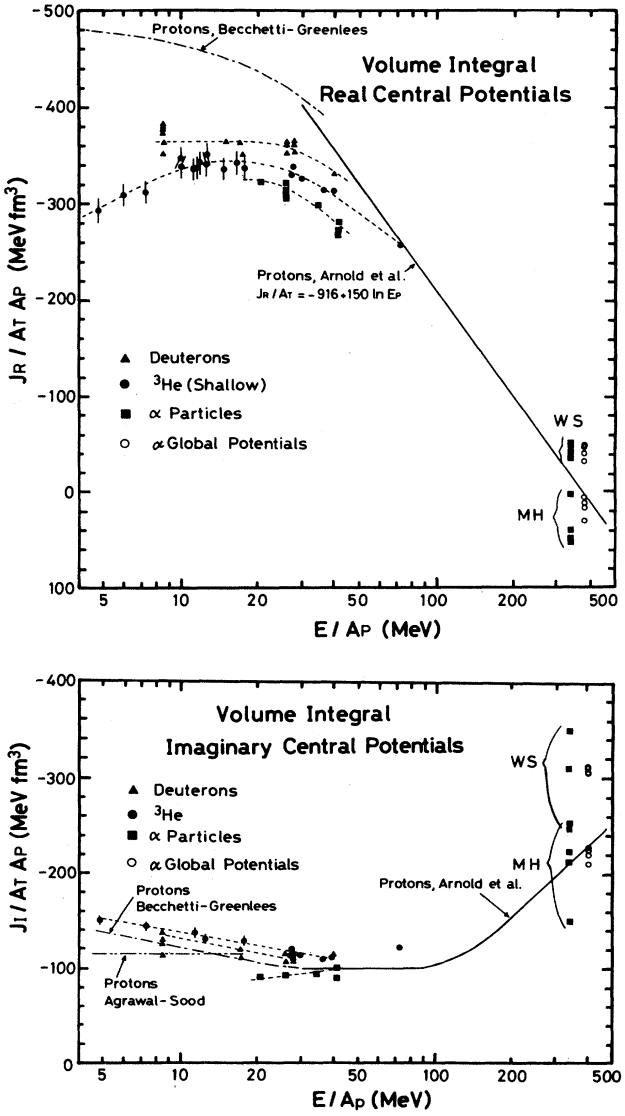

FIG. 12. Volume integrals of real (the upper panel) and imaginary (the lower panel) optical potentials together with Becchetti-Greenlees's and Arnold's lines which are suggested for proton scatterings, where WS and MH mean Woods-Saxon potentials and Mexican-hat potentials, respectively. The squares show volume integrals of the best-fit potentials and the open circles show those of the global potentials for $^{40,42,44,48}Ca$.

IV. CONCLUSIONS

In this paper, we have examined the application of optical models for the scattering of 1.37 GeV alpha particles on $^{40,42,44,48}Ca$ isotopes. Traditional Woods-Saxon and double-Woods-Saxon-type potentials were tried. The simple best-fit criterion is satisfied by the two potential sets. However the notch test and minimum chi-square (χ^2) condition reveal that the results are not very sensitive to the real well depth in traditional WS form. The insensitivity to the real depth is likely due to the masking by the deep imaginary potential. On the contrary, the DWS form with a less deep imaginary potential is quite sensitive to the shape and depth of the real potential for distances up to 3 fm.

Various tests such as shape dependence of χ^2/N, depth of the imaginary potentials, global potentials, and the volume integrals of the potentials indicate that the Mexican-hat shape is favorable for an optical potential of alpha particles at this energy.

The crucial point of the evidence is the shape dependence of the χ^2/N which is shown in Fig. 9. The results of ^{48}Ca, ^{42}Ca, and ^{40}Ca on clearly favor the Mexican-hat shape. The lack of sensitivity, in the case of ^{44}Ca, is most likely due to sparcity of data points in the fifth maximum. It should be noted that the shape in the interior region becomes less ambiguous with data extended to larger angles.[16] In our case, it is especially important to define the heights of the fifth and sixth peaks. This is easily understood from the comparison of angular distributions calculated for both shapes, as shown in Figs. 3 and 5. The calculated angular distributions by the WS shape decrease very rapidly outside the range of the measured angles. On the other hand, the Mexican-hat shape potential gives high peaks even at larger angles.

We determined the global potentials with no free parameters for both shapes, assuming smooth isotope dependence of the potential parameters, and could obtain better global potentials for the MH shape than for the WS shape. The global potentials also indicate that the

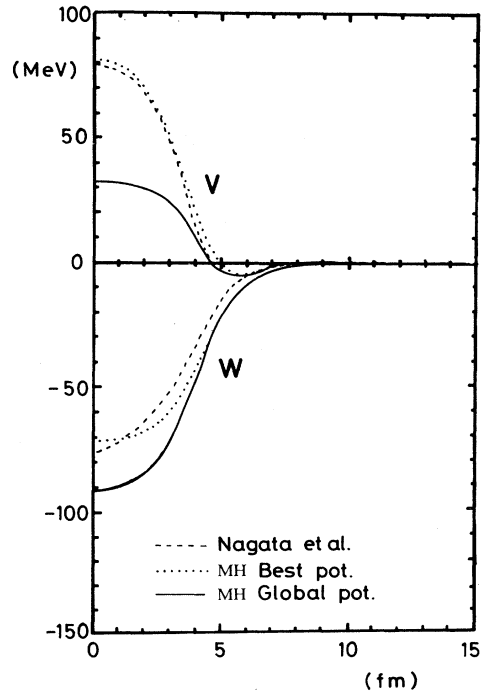

FIG. 13. Comparison of three kinds of the optical potentials in ^{40}Ca. The dotted and the solid lines show the best-fit MH potential and the global MH potential, respectively. These are phenomenologically obtained. On the other hand, the potential calculated by Nagata *et al.* is shown with the dashed line. For details, see Refs. 17–19.

MH shape is superior.

There is little difference between the global MH potentials and the best-fit MH potentials in the region larger than 4 fm. All the best-fit MH and the global MH potentials change sign around 5 fm from attractive to repulsive, and the depth of the attraction is less than 5 MeV. It should again be noted that the repulsion and the weak attraction in the surface region larger than 4 fm, which the Mexican-hat shape has, plays an important role in reproducing the high peaks at the backward angles in the angular distribution.

From theoretical points of view, the Mexican-hat shape is also supported for the potential at this energy. On the basis of the Brueckner theory, Nagata *et al.* succeeded in reproducing angular distributions of p-nucleus scatterings.[17] In their model, the optical potential is constructed[18] by folding the complex reaction G matrices, calculated in nuclear matter, into both density distributions of a target nucleus and a projectile. The optical potential[19] of the $\alpha+^{40}$Ca system at the energy of 343 MeV/nucleon is a typical Mexican-hat shape, which is similar to our best-fit potential as shown in Fig. 13, where the calculated potential is presented together with the best-fit and global MH potentials for ^{40}Ca.

Therefore we conclude that the optical potential analysis is applicable for the elastic scattering even at this energy, and the Mexican-hat shape is strongly suggested as a reasonable potential which should be adopted for the scattering of alpha particles at intermediate energies around 300 MeV/nucleon. This conclusion, together with the result of Ref. 6, indicates the fact that the potential shape changes systematically from a Woods-Saxon shape at low energies via a wine-bottle-bottom shape at around 100 MeV/nucleon to a Mexican-hat shape at 343 MeV/nucleon. It thus appears that alpha particle scattering also exhibits a gradual potential shape change with increasing energy, just as the proton and deuteron projectiles do.

ACKNOWLEDGMENTS

The authors would like to express their thanks to Professor G. Bruge and Dr. B. Bonin for providing much information on the scattering data at intermediate energies. The authors also wish to thank Professor S. Nagata and Professor N. Yamaguchi for informing us of their calculated results of the $\alpha+^{40}$Ca system at 1.37 GeV prior to publication. Thanks are also due to Dr. Iseri for providing the program code ALPS, a modified version of which we employed for numerical calculations. The authors would like to thank Professor C. Rangacharyulu for a careful reading of this manuscript.

[1]H. O. Meyer, P. Schwandt, G. L. Moake, and P. P. Shngh, Phys. Rev. C **23**, 616 (1981).

[2]L. R. B. Elton, Nucl. Phys. **89**, 69 (1966).

[3]P. Schwandt, in *Proceedings of the RCNP International Symposium on Light Ion Reaction Mechanism, Osaka, 1983,* edited by H. Ogata, T. Kammuri, and I. Katayama (RCNP, Osaka University, Osaka, Japan, 1983), p. 3.

[4]N. V. Sen, Y. Yanlin, J. Arvieux, G. Gaillard, B. Bonin, A. Boudard, G. Bruge, J. C. Lugol, T. Hasegawa, F. Soga, L. E. Antonuk, J. M. Cameron, S. T. Lam, G. C. Neilson, G. Roy, D. M. Sheppard, and R. Babinet, Nucl. Phys. **A464**, 717 (1987).

[5]B. Bonin, N. Alamanos, B. Berthier, G. Bruge, H. Faraggi, J. C. Lugol, W. Mittig, L. Papineau, A. I. Yavin, J. Arvieux, L. Farvacque, M. Buenerd, and W. Bauhoff, Nucl. Phys. **A445**, 381 (1985).

[6]T. Maki, H. Matsuura, M. Nakano, H. Ohgaki, and M. Matoba, *Abstract book of XI International Conference on Particles and Nuclei, Kyoto, 1987* (KEK, Ibaraki, Japan, 1987), p. 508.

[7]G. D. Alkhazov, T. Bauer, R. Bertini, L. Bimbot, O. Bing, A. Boudard, G. Bruge, H. Catz, A. Chaumeaux, P. Couvert, J. M. Fontaine, F. Hibou, G. J. Igo, J. C. Lugol, and M. Matoba, Nucl. Phys. **A280**, 365 (1977).

[8]R. J. Glauber, *High Energy Collision Theory,* in *Lectures in Theoretical Physics* (Interscience, New York, 1959), Vol. 1, pp. 315–414.

[9]R. Beurtey, M. Matoba, and J.-P. Tabet, Nucl. Instrum. Methods **153**, 297 (1978).

[10]C. M. Perey and F. G. Perey, At. Data Nucl. Data Tables **17**, 1 (1976).

[11]J. P. Jeukenne, A. Lejeune, and C. Mahaux, Phys. Rev. C **10**, 1391 (1974).
[12]J. C. Peng, R. M. Devries, and N. J. Digiacomo, Phys. Lett. **98B**, 244 (1981).
[13]M. Matoba, Phys. Lett. **56B**, 332 (1975).
[14]M. Matoba, M. Hyakutake, and I. Kumabe, Phys. Rev. C **32**, 1773 (1985).
[15]L. G. Arnold, B. C. Clark, E. D. Cooper, H. S. Sherif, D. A. Hutcheon, P. Kithcing, J. M. Cameron, R. P. Liljestrand, R. N. MacDonald, C. A. Miller, G. C. Neilson, W. C. Olsen, D. M. Sheppard, G. M. Stinson, D. K. McDaniels, J. R. Tinsley, R. L. Mercer, L. W. Swensen, P. Schwandt, and C. E. Stronach, Phys. Rev. C **25**, 936 (1982).
[16]M. Hyakutake, M. Matoba, I. Kumabe, M. Fukuda, T. Komatsuzaki, T. Yamagata, M. Tanaka, M. Inoue, I. Miura, and H. Ogata, Nucl. Phys. **A311**, 161 (1978).
[17]N. Yamaguchi, S. Nagata, and T. Michiyama, Prog. Theor. Phys. **76**, 1289 (1986).
[18]S. Nagata, M. Kamimura, and N. Yamaguchi, Prog. Thoer. Phys. **73**, 512 (1985).
[19]S. Nagata and N. Yamaguchi, private communication. The accuracy of their effective interaction (CEG) is ensured below about 200 MeV/nucleon. They constructed the folding potential in Fig. 13 by multiplying the factor 1.1 to all strengths of the third range of the real part in CEG interaction. The imaginary potential in Fig. 13 is calculated with CEG at 250 MeV/nucleon because the potential is considered to have weak dependence on the incident energy at these energies.